AAS 25-716

HETEROCLINIC TRANSFER BETWEEN L1 AND L3 IN EARTH-MOON SYSTEM

Abdullah Braik* **and Shane D. Ross†**

In this study, we explore the existence of heteroclinic transfers between Lyapunov orbits around the L1 and L3 points in the Earth-Moon system using the Planar Circular Restricted Three-Body Problem (PCR3BP) model. While transfers involving L1 and L2 have been extensively studied, transfers to L3 remain underutilized despite their potential benefits for long-term observation and low stationkeeping requirements. By computing Lyapunov orbits and their associated invariant manifolds, Poincaré maps are constructed to identify potential heteroclinic connections. Using this method, two transfer trajectories were found in each energy level. Those trajectories differ in their travel time between L1 and L3.

INTRODUCTION

A new era of deep-space exploration and cislunar operations is driving renewed interest in advanced trajectory design. NASA's Artemis program—with its planned Gateway lunar station—exemplifies the push for sustained human presence at the Moon and beyond.[1] In parallel, mission concepts like the Asteroid Redirect Mission (ARM) have been proposed to robotically capture a near-Earth asteroid and park it in lunar orbit for astronaut exploration and technology demonstrations.[2] At the same time, strategic interests are expanding beyond geosynchronous orbit: the need for cislunar space domain awareness has prompted studies of surveillance constellations in the Earth–Moon system to monitor the anticipated surge in spacecraft traffic.[3] Together, these developments underscore the importance of efficient transfer trajectory design in multi-body regimes to enable robust and cost-effective deep-space missions.

Efficient transfers in the Earth-Moon system hinge on exploiting its multi-body dynamical structure. In contrast to conventional two-body Hohmann transfers, low-energy trajectories leverage the Circular Restricted Three-Body Problem (CR3BP) dynamics to reduce ΔV expense. The Earth–Moon CR3BP hosts five equilibrium points (L_1–L_5) whose associated invariant manifolds form a network of pathways for ballistic transfers.[4] Past missions have validated this approach: for example, the CAPSTONE mission recently navigated a ballistic lunar transfer that followed natural gravitational contours to achieve lunar capture with minimal propellant.[5] By leveraging such multi-body dynamical routes, mission designers can attain transfers that would be infeasible or prohibitively costly in a patched two-body context.

Within this framework, heteroclinic transfers represent an especially elegant class of low-energy trajectories. A heteroclinic connection is a trajectory that asymptotically departs one invariant orbit (along that orbit's unstable manifold) and approaches another invariant orbit (along the stable manifold of the second orbit). In essence, the spacecraft "slides" from one libration-point orbit to another with no insertion burn at the junction.[6] This concept has since become a powerful paradigm for designing low-energy pathways through the coupled gravitational landscape of the CR3BP. By exploiting heteroclinic connections, missions can access distant or otherwise inaccessible orbits at negligible fuel cost, provided the timing and energy levels are matched.

To date, most applications of CR3BP transfers in the Earth–Moon system have focused on the L_1 and L_2 libration point regions. Extensive surveys and mission studies have characterized halo orbits around L_1/L_2,[7]

*PhD Student, Aerospace and Ocean Engineering, Virginia Tech, Blacksburg, VA, USA, braik@vt.edu
†Professor, Aerospace and Ocean Engineering, Virginia Tech, Blacksburg, VA, USA, sdross@vt.edu

stationkeeping strategies,[8] and transfers between these orbits.[9] Notably, NASA's ARTEMIS mission was the first to maneuver spacecraft into Earth–Moon L_1 and L_2 orbits, demonstrating the practical feasibility of low-energy libration-point transfers.[10] In contrast, the Earth–Moon L_3 point has received relatively little attention. Situated on the opposite side of Earth from the Moon, Earth–Moon L_3 has not yet been utilized by any mission, and early trajectory research largely overlooked it in favor of the nearer and more accessible L_1/L_2 regions. However, there is a growing recognition that L_3's underexplored location offers unique value for future operations.

Several factors make a compelling case for renewed focus on Earth–Moon L_3. First, dynamical analyses show that L_3 is quasi-stable, exhibiting lower unstable eigenvalues compared to L_1 and L_2. Volta and Vaughn[11] showed that certain periodic orbits around Earth–Moon L_3 can remain stable for up to 250 days without control. Second, L_3's remote location and broad vantage point confer strategic advantages for cislunar situational awareness. A vehicle in an L_3 halo orbit is well-positioned for surveillance, offering line-of-sight views of regions on Earth that are otherwise hidden from ground sensors or L_1/L_2 assets. Recent studies have considered Earth–Moon L_3 orbits as potential "watchpoints" for monitoring activities in cislunar space, in conjunction with satellites around L_4 and L_5.[12] Another study considers that a constellation of satellites in L_1,L_2 and, L_3 halo orbits would provide continuous lunar global positioning and navigation services, with L_3 satellites requiring the lowest maintenance cost ($\Delta V = 0.02m/s$ over 60 days)."[13] Additional investigations have further highlighted the utility of L_3 orbits in cislunar logistics and transfer architectures. For instance, Liang et al. demonstrated how stable and unstable manifolds associated with Earth–Moon L_3 can facilitate low-energy transfers to triangular libration points, showcasing L_3 as a dynamic hub in mission designs.[14] Additionally, Evans et al. highlight the strategic importance of mapping transfers from L_3 to Earth orbit to support future return trajectories, situational awareness, and cislunar traffic management.[15] Third, L_3 could serve as an effective staging area for missions like near-Earth object (NEO) capture and redirect.[16] Invariant manifolds associated with L_3 connect naturally to the Sun–Earth domain, facilitating low-energy insertion of objects into cislunar space. As a concrete example, Jorba and Nicolás[17] demonstrate that a small asteroid (e.g., 2006 RH120) can be transferred into an Earth–Moon L_3 orbit with a ΔV of only ≈ 20 m/s by aligning with L_3's stable manifold—an extraordinarily low cost that showcases L_3's potential as a capture point for interplanetary material.

Despite these advantages, heteroclinic transfers involving the L_3 region have not been previously explored in the literature, leaving a gap in multi-body trajectory design knowledge. In this paper, we address that gap by demonstrating the existence of heteroclinic connections between L_1 and L_3 periodic orbits in the Earth–Moon system. Using the planar CR3BP model, we compute and analyze two distinct families of heteroclinic transfers—denoted $\mathcal{H}^+$ and $\mathcal{H}^-$—linking Lyapunov orbits around L_1 to their counterparts around L_3. These families correspond to two distinct heteroclinic trajectories that follow different routes through the Earth–Moon system before converging to the target orbit. We characterize the geometry of these connections in configuration and phase space and examine their time-of-flight and phasing requirements. The results reveal rich transfer opportunities between L_1 and L_3, enabled by the intersections of invariant manifold tubes. By identifying and cataloging these $L_1 \rightarrow L_3$ heteroclinic pathways, the present work expands the toolbox for low-energy mission design in cislunar space—opening the L_3 region to practical use through natural dynamical bridges from the well-studied L_1 vicinity.

PLANAR CIRCULAR RESTRICTED THREE BODY PROBLEM

The model used in this study is the planar circular restricted three-body problem (PCR3BP). The model simplifies the true three-body problem while capturing the main qualitative dynamics. It describes the motion of an object under the influence of the gravitational force of two larger bodies (e.g., Earth and Moon). The simplification is achieved by the following assumptions: (i) the object is massless; (ii) the two primary bodies are in a circular motion around their barycenter with a constant angular velocity, viewed in a rotating frame; and (iii) the object moves in the plane of the two primary bodies.

Equations of Motion in PCR3BP

In this model, the equations of motion are described in a rotating frame. Also, they are normalized such that the distance between the two larger masses is 1, their total mass $(m_1 + m_2)$ is 1, and the sidereal period,

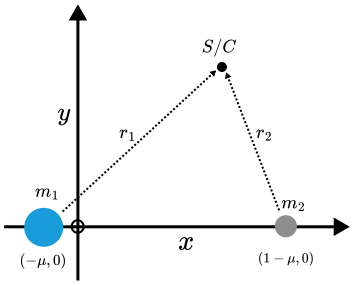

Figure 1: Planar Circular Restricted Three-Body Problem Configuration

T_m, is 2π. Therefore, the only parameter of the system dynamics is the mass ratio, μ, which is defined as $\mu = \frac{m_2}{(m_1+m_2)}$. The rotating frame is selected such that the barycenter of the primaries is at the origin and m_1 and m_2 are located on the x-axis at $(-\mu, 0)$ and $(1-\mu, 0)$, respectively. The configuration is shown in Figure 1. The PCR3BP equations of motion in normalized units are,

$$\ddot{x} - 2\dot{y} = -\frac{\partial \bar{U}}{\partial x}, \quad \ddot{y} + 2\dot{x} = -\frac{\partial \bar{U}}{\partial y}, \tag{1}$$

where $\bar{U}$ is the effective potential, defined as,

$$\bar{U}(x, y) = -\frac{1}{2}(x^2 + y^2) - \frac{1-\mu}{r_1} - \frac{\mu}{r_2} \tag{2}$$

where $r_1 = \sqrt{(x+\mu)^2 + y^2}$ and $r_2 = \sqrt{(x-1+\mu)^2 + y^2}$ are the distance of the spacecraft from m_1 and m_2, respectively.

Jacobi Constant and Zero Velocity Curves

The Jacobi constant is the sole integral of motion in the CR3BP, and is proportional to the system's Hamiltonian energy. It is defined by,

$$C(x, y, \dot{x}, \dot{y}) = -2\bar{U}(x, y) - (\dot{x}^2 + \dot{y}^2). \tag{3}$$

The level sets of C define the allowed and forbidden regions in configuration space, bounded by what are known as zero velocity curves (ZVCs). These curves mark the loci where the velocity magnitude in the rotating frame, $\sqrt{\dot{x}^2 + \dot{y}^2}$, is zero, and hence delineate the boundaries beyond which a particle with a given C cannot pass. As the Jacobi constant varies, the topology of these regions changes, opening or closing transit corridors between different dynamical regions.

At each equilibrium (Lagrange) point L_i, the effective potential $\bar{U}$ attains a critical value $\bar{U}_i$, corresponding to a critical Jacobi constant,*

$$C_i = -2\,\bar{U}_i. \tag{4}$$

For $C > C_1$, all ZVCs are closed around the Earth and Moon, isolating their respective dynamical regions. As C decreases to C_1, a narrow "neck" opens at L_1, creating the first possible transit passage. Further decreases to C_2 and C_3 open additional necks at L_2 and L_3, respectively, as well as eventually connecting to the exterior region beyond the primaries. Table 1 summarizes the critical Jacobi constants for each of the five Lagrange points.

This progressive opening and closing of dynamical gateways at the equilibrium points forms the backbone of low-energy transfers. Since this study is focused on heteroclinic transfers between L_1 and L_3, we restrict our analysis to Jacobi constants satisfying $C < C_3$.

*This definition differs from other authors, who add a constant $\mu(1-\mu)$, to have the Jacobi Constant at L_4 and L_5 exactly 3. We dropped this constant in this study to match the current use among the cislunar astrodynamics community.

Table 1: Critical Jacobi Constants C_i at Lagrange Points L_i

L_i	C_i
L_1	3.1883
L_2	3.1722
L_3	3.0122
L_4	2.9880
L_5	2.9880

Lyapunov Orbits and Invariant Manifolds

Linearization of the PCR3BP about each collinear equilibrium point (L_1, L_2, and L_3) yields a pair of real and a pair of purely imaginary eigenvalues. By the Lyapunov center theorem, this structure guarantees the existence of a continuous family of planar, symmetric periodic solutions—known as Lyapunov orbits—bifurcating from each L_i.

For each L_i, there exists a one-parameter family of such orbits, typically parameterized by the Jacobi constant (or equivalently, by the orbit's amplitude or period). These orbits lie entirely in the rotating frame's plane and are symmetric about the x-axis. As the Jacobi constant decreases further below C_i, the Lyapunov orbit grows in size and its period changes smoothly. Because they lie just inside the neck openings of the ZVCs around L_i, Lyapunov orbits serve as dynamical gateways between different regions of motion.

Each Lyapunov orbit is a hyperbolic periodic orbit. The monodromy matrix of its linearization has one real eigenvalue outside the unit circle (unstable) and one inside (stable), plus two neutral eigenvalues at unity corresponding to phase shifts along the orbit and nearby periodic solutions with different Jacobi constants. The unstable invariant manifold of a Lyapunov periodic orbit is the set of trajectories that asymptotically approach the periodic orbit as $t \to -\infty$, while the stable invariant manifold consists of trajectories that asymptotically approach the orbit as $t \to +\infty$.

When these manifolds intersect a suitable Poincaré section, they appear as one-dimensional closed curves. A heteroclinic connection is a trajectory that lies on both the unstable manifold of one Lyapunov orbit and the stable manifold of another. On the Poincaré section, this corresponds to an intersection point between the two closed curves, indicating a natural, control-free transfer trajectory between the associated periodic orbits.

Poincaré Sections

A Poincaré section is a classical tool in dynamical systems for reducing continuous-time flows to discrete-time mappings. One selects a co-dimension-1 "surface of section" Σ_C in the 3-dimensional level set of C and records the state each time a trajectory intersects that surface (usually only when crossing in a given direction, but see below). By plotting these intersection points in an appropriate 2D subspace, one obtains a representation that captures the essential structure of the underlying flow: periodic orbits appear as fixed points, invariant tori as closed curves, and the stable and unstable manifolds of hyperbolic orbits as distinct traceable curves whose intersections signal possible phase-space connections.

In our Earth–Moon heteroclinic study, we exploit a Poincaré section to reduce the four-dimensional phase space of the planar CR3BP (two positions and two velocities) to a two-dimensional discrete representation. We define the surface-of-section,

$$\Sigma_C = \{(y, \dot{y}) \mid x = -\mu,\ C(x, y, \dot{x}, \dot{y}) = \text{constant}\}, \tag{5}$$

in the rotating frame. Each crossing is recorded by its $(y, \dot{y})$ coordinates, yielding a 2D scatter plot of points along trajectories. Overlaying the closed curve of a stable manifold of an L_1 Lyapunov orbit with the closed curve of an unstable manifold of an L_3 Lyapunov orbit on this $(y, \dot{y})$ plane reveals locations where natural, zero-ΔV transfers are possible; namely, at the intersection points of these two closed curves.

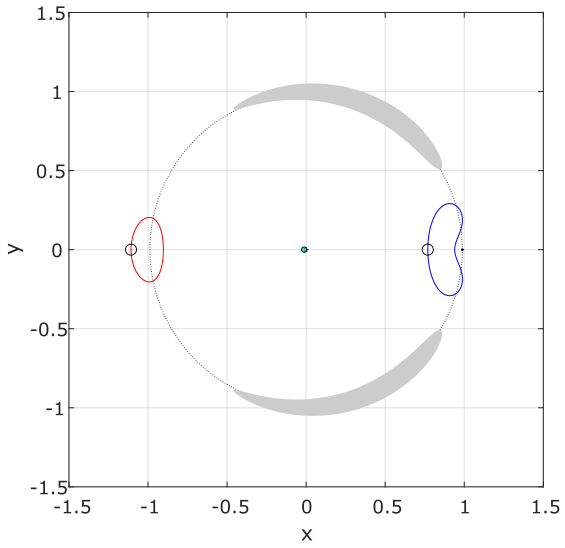

Figure 2: Lyapunov orbits at $C = 3.0010$: L_3 (red) and L_1 (blue), with the ZVC in gray (rotating frame). Necks around both L_3 and L_1 are open. Lunar orbital radius shown for reference.

METHODOLOGY

Selection of Jacobi Constant

The first step in generating a heteroclinic transfer is the selection of an appropriate Jacobi constant. As shown in Table 1, the critical Jacobi constant at L_3 is $C_3 = 3.0122$. Any value of $C < C_3$ opens the ZVC around L_3, thereby permitting the existence of a Lyapunov orbit in that region. However, the mere existence of both L_1 and L_3 Lyapunov orbits is not sufficient to guarantee a heteroclinic connection between them.

A second requirement is the existence of an intersection between the stable and unstable manifolds of the selected Lyapunov orbits on the chosen Poincaré section. Through numerical exploration, we find that such manifold intersections only occur for,

$$C < C_{\max} \approx 3.0015, \tag{6}$$

where $C_{\max}$ represents the upper bound on Jacobi constants that support any $L_1 \to L_3$ or $L_3 \to L_1$ heteroclinic connection.

Figure 2 shows representative L_3 (red) and L_1 (blue) Lyapunov orbits at $C = 3.0010$, together with the ZVC (boundary of gray regions) in the rotating frame. Both necks near L_1 and L_3 are visibly open, allowing for the possibility of transit and enabling the search for heteroclinic trajectories in this energy regime.

Lyapunov Orbit Generation

To initialize each Lyapunov orbit computation, we obtain the state vector $(x_0^g, y_0^g, \dot{x}_0^g, \dot{y}_0^g)$ and associated period T^g directly from the JPL Three-Body Periodic Orbit Database.[18] These values serve as initial guesses for the differential correction procedure. Typically, the Jacobi constant implied by the JPL solution, C_{JPL}, differs slightly from the desired target value C_{target}.

Since a true heteroclinic connection requires both Lyapunov orbits to reside on the same energy surface (i.e., to share an identical Jacobi constant), even a small mismatch in C will place their invariant manifold tubes on distinct level sets, preventing a natural transfer between them. Consequently, a differential correction step is indispensable. We perturb the initial x-position and recompute $\dot{y}_0$ to enforce the energy constraint,

$$C(x_0, 0, 0, \dot{y}_0) = C_{\text{target}}, \tag{7}$$

thereby ensuring that both L_1 and L_3 Lyapunov orbits lie on the same Jacobi manifold within a specified tolerance, enabling a true heteroclinic connection.

To enforce periodicity, we exploit the time-reversal symmetry of the CR3BP in the rotating frame. Lyapunov orbits are symmetric about the x-axis; thus, at half their period they cross the x-axis perpendicularly (i.e., $\dot{x} = 0$). Starting from the JPL-provided initial guess, we integrate forward from $t = 0$ until the trajectory first intersects the x-axis with $\dot{y} < 0$, which occurs at some time t_1. At this point, we impose the vertical crossing conditions,

$$y(t_1) = 0, \quad \dot{x}(t_1) = 0, \tag{8}$$

which reduces the boundary-value problem to a single unknown: the corrected value of x_0. We then apply Newton–Raphson iterations to update x_0, recomputing $\dot{y}_0$ at each step to maintain $C = C_{\text{target}}$, until $|\dot{x}(t_1)|$ falls below a prescribed convergence threshold, $\varepsilon_L \ll 1$. For this study the threshold was chosen to be $\varepsilon_L = 10^{-12}$.

The correction loop is as follows:

1. **Initialization.** Choose an initial guess,

   $$X_0^g \;=\; \big(x_0^g,\, 0,\, 0,\, \dot{y}_0^g\big), \quad C_{\text{target}}, \quad t_{\min}, \quad \varepsilon_L, \text{ and set the iteration number } n = 1.$$

2. **Propagate to half-period.** Integrate the equations of motion and the STM, $\dot{\Phi} = Df(X)\,\Phi,\ \Phi(0) = I$, from $t = 0$ until the first crossing (t_1) of,

   $$y = 0, \quad \dot{y} < 0, \quad t > t_{\min},$$

   yielding

   $$t_1^{(n)}, \quad X\big(t_1^{(n)}\big) = \big(x_1,\ 0,\ \dot{x}_1,\ \dot{y}_1\big), \quad \Phi\big(t_1^{(n)}, 0\big).$$

3. **Form Newton–Raphson update.** Define the velocity error

   $$e = \dot{x}_1\,.$$

   The correction δx_0 is obtained by linearizing $\dot{x}_1$ with respect to the initial x_0. In closed form:

   $$\delta x_0 = \dot{x}_1 \left(\frac{\dot{y}_1}{\ddot{x}_1\,\Phi_{21}}\right)\Big[1 - \frac{\Phi_{24}}{\Phi_{21}}\frac{1}{\dot{y}_0^{g(n)}}\frac{\partial \bar{U}}{\partial x}(x_0^g, 0) - \frac{\dot{y}_1}{\ddot{x}_1\,\Phi_{21}}\Big(\Phi_{31} - \Phi_{34}\frac{1}{\dot{y}_0^{g(n)}}\frac{\partial \bar{U}}{\partial x}(x_0^g, 0)\Big)\Big]^{-1},$$

   where $\Phi_{ij} = \Phi_{ij}(t_1^{(n)})$ is the i^{th} row and j^{th} column entry of Φ, $\ddot{x}_1 = 2\dot{y}_1 - \partial U/\partial x\big(x_1, 0\big)$, and $\dot{y}_0^{g(n)}$ is the current guess of $\dot{y}$ at $t = 0$.

4. **Update initial conditions & enforce energy.**

   $$x_0^{g(n+1)} = x_0^{g(n)} - \delta x_0, \qquad \dot{y}_0^{g(n+1)} = +\sqrt{-2\,\bar{U}\big(x_0^{g(n+1)},\, 0\big) - C_{\text{target}}}\,,$$

   choosing the "+" sign so that $\dot{y}_0 > 0$.

5. **Convergence check.** If $|e| < \varepsilon_L$, the orbit converges and we set $x_0 = x_0^{g(n+1)},\ y_0 = y_0^{g(n+1)}$. Otherwise, increment $n \to n + 1$ and return to step 2.

Once the solution has converged, we obtain a Lyapunov periodic orbit with the targeted Jacobi constant. This orbit forms the basis for generating its associated invariant manifolds.

Using the correction approach described above, families of Lyapunov orbits around both L_1 and L_3 can be systematically constructed across a range of Jacobi constants. Figure 3a shows representative orbit families for L_3 (left) and L_1 (right), with each orbit colored according to its Jacobi constant. Figure 3b shows the associated orbital periods of the Lyaponuv Orbits Families. Across the selected C-range, the L_3 family's period remains essentially fixed at approximately 27 days—despite changes in orbit size—whereas the L_1 family's period decreases steadily with increasing C, reflecting its shrinking Lyapunov orbits.

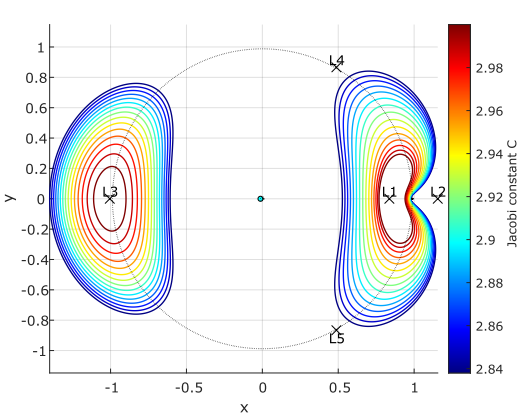

(a) L_3 (on left) and L_1 (on right) Lyapunov orbits colored by their Jacobi constant, C.

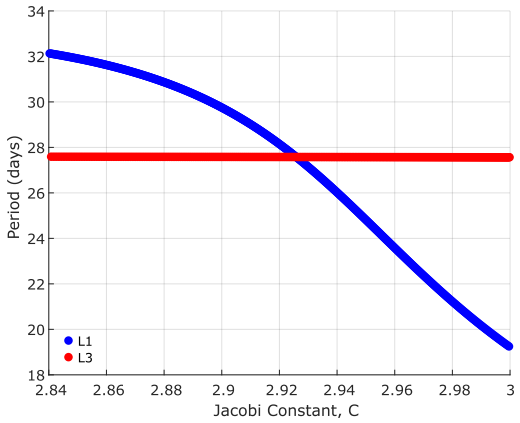

(b) L_1 (Blue) and L_3 (Red) orbital periods; L_3 period is constant throughout and L_1 period decrease with C.

Figure 3: L_3 and L_1 Lyapunov orbits

Invariant Manifold Computation

Along each converged Lyapunov orbit,

$$\mathbf{X}(t), \quad 0 \le t \le T,$$

we integrate the variational equation,

$$\dot{\Phi}(t) \;=\; Df\big(\mathbf{X}(t)\big)\,\Phi(t), \qquad \Phi(0) = I_{4\times 4}, \tag{9}$$

over one full period T. The resulting monodromy matrix $\Phi(T)$ encodes the linear mapping of infinitesimal perturbations after one orbit. We compute its eigenvalues $\{\lambda_i\}$ and eigenvectors $\{v_i\}$, identifying the real pair $\lambda_u > 1$ (unstable) with eigenvector v_u and the reciprocal $\lambda_s = 1/\lambda_u < 1$ (stable) with eigenvector v_s.

To seed the invariant manifolds, we sample the orbit at N evenly spaced phase-fractions,

$$\tau_k = \frac{k-1}{N-1}, \quad k = 1, \ldots, N, \tag{10}$$

so $\tau_1 = 0$ and $\tau_N = 1$. At each τ_k we evaluate the state an STM at fraction point k,

$$\mathbf{X}_k = \mathbf{X}(\tau_k T), \qquad \Phi_k = \Phi(\tau_k T), \tag{11}$$

by integrating (9) from 0 to $\tau_k T$. The local linear approximation to the manifold at $\mathbf{X}_k$ is,

$$\Delta\mathbf{X}_k = \Phi_k\, v_{s/u}, \tag{12}$$

where one uses v_s for the stable manifold and v_u for the unstable. We split $\Delta\mathbf{X}_k = (\Delta\mathbf{r}_k, \Delta\mathbf{v}_k)$, rescale to a fixed small amplitude ε_M via,

$$\Delta\mathbf{X}'_k = \frac{\varepsilon_m}{\|\Delta\mathbf{r}_k\|}\,\Delta\mathbf{X}_k, \tag{13}$$

so that $\|\Delta\mathbf{r}'_k\| = \varepsilon_M$. In practice $\varepsilon_M = 10^{-6}$ (≈ 0.384 km) and N based on the amplitude of the orbit to balance resolution and computational cost.

Finally, we form two seeds on each side of the orbit,

$$\tilde{\mathbf{X}}^{\pm}_k = \mathbf{X}_k \;\pm\; \Delta\mathbf{X}'_k. \tag{14}$$

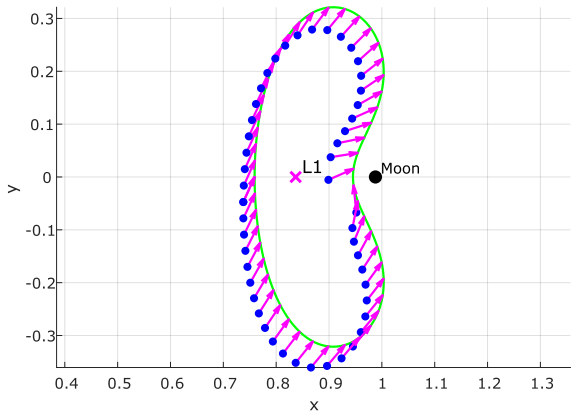

Figure 4: the "$-$" stable manifold branch seeding for L_1 Lyapunov Orbit

where the "$+$" and "$-$" branches sample both sides of the manifold tube, with the "$+$" branch following the manifold in the general direction of increasing x and the "$-$" branch in the direction of decreasing x. When these seeds are integrated forward in time (unstable) or backward in time (stable), they trace out the full four-dimensional invariant manifold used for intersection detection and heteroclinic-transfer construction.

Figure 4 illustrates the configuration-space seeding for the stable manifold of the L_1 Lyapunov orbit. The green curve traces the periodic orbit itself. At each sampled phase fraction, the magenta arrow indicates the local stable direction obtained by transporting the Floquet eigenvector via the STM. The blue dots mark the actual seed points $\tilde{\mathbf{X}}_k^- = \mathbf{X}_k - \Delta\mathbf{X}'_k$ on the "$-$" branch of the stable manifold. For clarity of illustration, the deviation amplitude ϵ has been artificially exaggerated relative to its true value.

Poincaré Section Recording

In prior studies of Earth–Moon equilibrium point transfers, particularly between L_1 and L_2, Poincaré maps of manifold intersections are typically generated by recording a single crossing of each trajectory through a specified section with a prescribed direction of motion. A common choice is a vertical section at $x = 1 - \mu$ (near the smaller primary), where only crossings with $\dot{x} > 0$ are recorded. This single-crossing approach, employed in foundational analyses such as Koon et al.[19] and Gómez and Masdemont,[20] yields one unique point per trajectory on the section. Overlapping points from the stable and unstable manifolds in such maps indicate potential heteroclinic connections.

While this method has proven effective for L_1–L_2 transfers, we found that it fails to capture the full manifold structure in the L_1–L_3 transfer scenario. When applying the single-crossing method to the "$-$" stable manifold branch of an L_1 Lyapunov orbit (W_1^{s-}) and the "$+$" unstable manifold of an L_3 orbit (W_3^{u+}), the resulting Poincaré map——using a section Σ_C defined at $x = -\mu$ (the Earth location in normalized coordinates)——exhibited large gaps in the distribution of intersection points in the section's $(y, \dot{y})$ projection. These gaps were particularly pronounced in regions where heteroclinic intersections were expected to occur. In other words, where we anticipated the Poincaré cuts of W_1^{s-} and W_3^{u+} to intersect, signaling viable transfer trajectories, the single-crossing map was underpopulated or entirely empty, undermining our ability to detect actual connections.

Closer inspection revealed the cause: many trajectories in both W_1^{s-} and W_3^{u+} exhibit localized "looping" behavior in configuration space. As a trajectory evolves, it may execute tight loops in the x–y plane, a natural feature of the flow at these energy levels. Crucially, when such loops occur near the section plane $x = -\mu$, the trajectory can pierce the section multiple times in rapid succession; first in one direction, then looping around and recrossing in the opposite direction shortly after.

Figure 5b shows a close-up of the manifold geometry depicted in Figure 5a, highlighting this phenomenon. Several trajectories from W_1^{s-} and W_3^{u+} loop near $x = -\mu$, resulting in successive intersections with the vertical section line as they reverse direction.

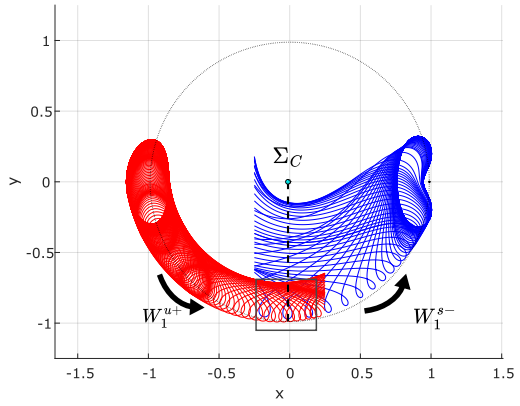

(a) Stable L_1 Manifold (Blue), Unstable L_3 Manifold (Red) and Poincaré Section Σ_C (Dashed line) at $C = 2.9880$. Region in gray box highlighted in panel b.

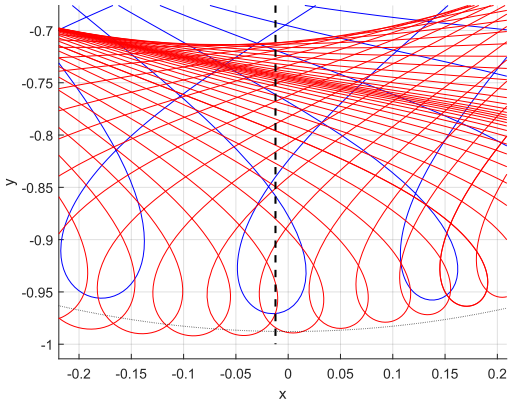

(b) Closer look at panel (a) (gray box) showing looping behavior near Σ_C.

Figure 5: Invariant Manifold and Loops

Under the conventional single-crossing method (recording only the first crossing with a prescribed $\dot{x}$ sign), most of these loop-induced piercings are missed. The algorithm records only the first instance that meets the directional condition (e.g., the first crossing of $x = -\mu$ with $\dot{x} > 0$) and ignores subsequent ones. The edges of the missing regions on the Poincaré map correspond to near-tangential crossings at $x = -\mu$ (i.e., when $\dot{x}$ approaches zero), a behavior directly linked to the looping trajectories described above. As a result, valid intersection points near the loops go unrecorded, producing wide gaps in the $(y, \dot{y})$ map, especially around the heteroclinic intersections of interest. This not only leads to discontinuities but also impedes interpolation, root finding, and optimization routines that require dense, continuous data on the section.

To resolve this, we implemented an enhanced two-event function strategy for recording manifold crossings with the Poincaré section. Each manifold trajectory (for both L_1-stable and L_3-unstable families) is propagated using the following logic:

1. **Multi-crossing section event:** An event is defined at Σ_C ($x = -\mu$) without any directional constraint. Every crossing of the trajectory through $x = -\mu$, regardless of the sign of $\dot{x}$, triggers a record of that state (projected onto the section). This ensures that all relevant piercings, including those caused by local loops, are captured in the map.

2. **Region-limited integration:** Each manifold trajectory is terminated once it exits a predefined region of interest around Σ_C. These integration bounds (defined by x limits) are selected to include the local neighborhood where looping occurs, but to exclude distant re-crossings. This prevents the map from being cluttered with unrelated or long-return intersections, keeping the focus on near-Earth heteroclinic structure.

Applying this two-step Poincaré mapping strategy yields a significantly more complete set of manifold intersections on Σ_C. Figure 6b illustrates the improvement. The previously missing regions of the $(y, \dot{y})$ map are now filled with manifold points—blue for W_1^{s-} and red for W_3^{u+}—revealing numerous overlaps that indicate true heteroclinic connections between L_1 and L_3 Lyapunov orbits. However, because of the regions of the tangencies, small segments of the manifold traces remain under-resolved even in the multi-crossing map. Nonetheless, the critical heteroclinic intersections that were missing in the single-crossing map (Figure 6a) are now clearly visible.

By allowing multiple section piercings per trajectory, while bounding integration to a region of interest, this enhanced mapping strategy fully reveals the geometry of the L_1–L_3 manifold intersections on the Poincaré section. It enables robust detection of heteroclinic connections and enhances the design of low-energy transfers in this previously underexplored regime.

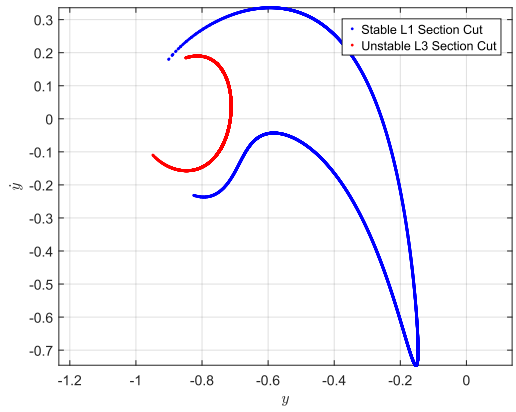

(a) Poincaré map using the traditional single-direction crossing criterion. Large gaps appear in key regions.

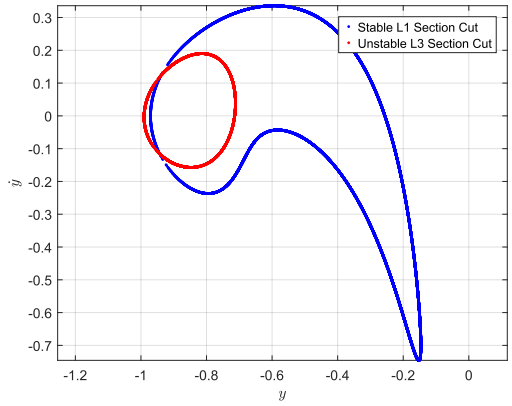

(b) Poincaré map using the multi-crossing approach, capturing all crossings in the region of interest.

Figure 6: Comparison of single-crossing and multi-crossing Poincaré mapping strategies on Σ_0.

HETEROCLINIC CONNECTION DETECTION

Heteroclinic Connection via Closest-Points Search

With the enhanced Poincaré mapping strategy in place, we now identify heteroclinic connections between L_1 and L_3 Lyapunov orbits in the Earth-Moon system. To accomplish this, we implement a closest-points search on the Poincaré map. For each value of the Jacobi constant C, the procedure is as follows:

1. **Generate Manifold Points:** Propagate a dense set of trajectories on W_1^{s-} (L_1 stable manifold) and W_3^{u+} (L_3 unstable manifold) and collect their $(y, \dot{y})$ coordinates at each crossing of the plane $x = -\mu$. This yield two sets of points that resemble a curve on the section (one for W_1^{s-} and another for W_3^{u+}).

2. **Compute Filtered Distances:** For each stable-manifold point p_s, compute its Euclidean distance in the $(y, \dot{y})$ plane to every unstable-manifold point p_u, *but only if* $\text{sign}(\dot{x}_s) = \text{sign}(\dot{x}_u)$. This ensures we only compare piercings that have the same direction of motion through the section.

3. **Identify Minimum:** Among all distance values computed above, select the pair $\{p_s, p_u\}$ with the smallest distance. This pair represents the closest, same-sign approach of W_1^{s-} and W_3^{u+}.

4. **Select Connection:** Treat this pair closest pair as a heteroclinic intersection. In other words, the trajectories corresponding to $\{p_u, p_s\}$ constitute a nearly continuous path from the vicinity of L_3 to the vicinity of L_1. By using the states associated with these and integrating forwards and backwards appropriately, a full trajectory can be constructed to represent the heteroclinic transfer.

This brute-force closest-point search reliably identifies near-intersections of the invariant manifolds. In essence, we assume that if W_3^{u+} and W_1^{s-} come sufficiently close in the Poincaré section, a true intersection is either present or can be obtained with a small adjustment. This assumption is justified by the fact that heteroclinic connections exist when the stable and unstable manifolds intersect on a common surface. In practical terms, if the minimum separation on the map is very small (below some tolerance), the corresponding manifold arcs for a low-energy transfer trajectory between L_1 and L_3. Hence, if the invariant manifolds did not come into proximity on the section, no natural heteroclinic transfer would be possible at that energy level. In our analysis, the smallest distance pair for each C was found to yield a feasible trajectory that connects the two regions, confirming that the closest approach criterion is sufficient for constructing full path solutions.

Remarks on Precision: The closest two-points approach provides a discrete approximation to the true intersection. A more rigorous approach would be to treat the manifold traces as continuous closed curves and solve for an exact intersection via a root-finding technique. For example, one could fit the smooth curves

through the discrete Poincaré points of W_3^{u+} and W_1^{s-} and then iterate to find where those two curves intersect exactly. From that intersection one can obtain two state $(y, \dot{y})$, x from the Poincaré section $x = -\mu$, and $\dot{x}$ from the Jacobi Constant definition $\dot{x}(C, x, y, \dot{y})$. Another approach is to use $\{p_u, p_s\}$ as an initial guess for a differential correction method to eliminate any small gap between them. Implementing such a curve-fitting and differential correction scheme is left for future work. For the purposes of this study, however, the simpler closest points strategy is adequate. The separation of $\{p_u, p_s\}$ in each case was negligible enough that corresponding trajectory segments could be patched together with minimal discrepancy.

Intersection Geometry on the Poincaré Map and Heteroclinic Construction

For every Jacobi constant examined, the filled $(y, \dot{y})$ section contains two distinct nearest-approach pairs of points between W_3^{u+} and W_1^{s-}. One lies at a positive $\dot{y}$ value, the other at a negative $\dot{y}$. Even though they share the same energy level, these two pairs are not mirror images of each other; they occur at different $(y, \dot{y})$ coordinates and correspond to genuinely different passages through the Earth-Moon region (their transfer geometries will be compared in the following section).

Starting from either of these two closest points, we construct a candidate heteroclinic trajectory by integrating the unstable-manifold state p_u backward in time and the stable-manifold state p_s forward in time until both arcs traverse the configuration space linking L_3 and L_1 Lyapunov orbits. Both integrations were carried out with a high-order Runge–Kutta scheme using an absolute and relative tolerance of 10^{-14}. The unstable arc spirals outward from the L_3 Lyapunov orbit until it reaches the stable arc which coasts towards the L_1 Lyapunov orbit and asymptotically approaches it. Therefore a practical heteroclinic transfer is formed and denoted:

$$\mathcal{H}_{3\to1}^{+} \text{ (for } \dot{y} > 0) \quad \mathcal{H}_{3\to1}^{-} \text{ (for } \dot{y} < 0) \tag{15}$$

Because of the time-reversal symmetry of the PCR3BP equations of motion,

$$(x, y, \dot{x}, \dot{y}, t) \longmapsto (x, -y, -\dot{x}, \dot{y}, -t), \tag{16}$$

each of the two physically distinct transfers $\mathcal{H}_{3\to1}^{+}$ and $\mathcal{H}_{3\to1}^{-}$ possesses a mirror image counterpart, $\mathcal{H}_{1\to3}^{+}$ and $\mathcal{H}_{1\to3}^{-}$, respectively, in configuration space, obtained by applying the symmetry. Because this symmetry reverses the invariant manifold's stability, it moves from the L_1 Lyapunov orbit to the L_3 Lyapunov orbit in the opposite side of the configuration space. Hence, for every Jacobi Constant C investigated, the dynamics admits four heteroclinic connections in total: the two computed directly from the closest pair procedure, and their two symmetric twins. For brevity, the discussion that follow concentrate on the explicitly calculated pairs; the time reversed solution inherit the same dynamical features from $\mathcal{H}_{3\to1}^{+}$ and $\mathcal{H}_{3\to1}^{-}$.

Figures 7 and 8 illustrate this geometry for $C = 2.9480$. Figure 7 shows the closest two pair $\{p_u, p_u\}^{\pm}$ represented on the previously generated $(y, \dot{y})$ section. Figure 8 represents their associated heteroclinic transfers $\mathcal{H}_{3\to1}^{\pm}$ and $\mathcal{H}_{1\to3}^{\pm}$ colored the same as the initial pair. One can notice that the constructed $\mathcal{H}_{3\to1}^{\pm}$ trajectories behave differently, even though they are on the same lower half of the plane.

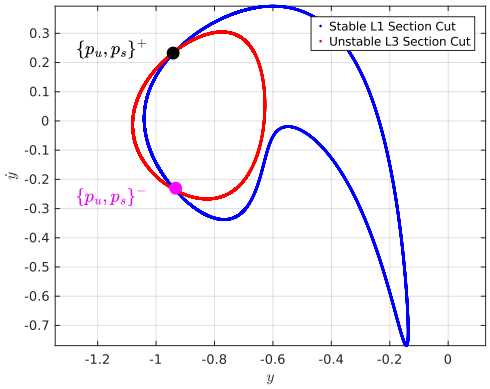

Figure 7: Poincaré map Σ_C showing closest pairs $\{p_u, p_s\}^{\pm}$ at $C = 2.9480$

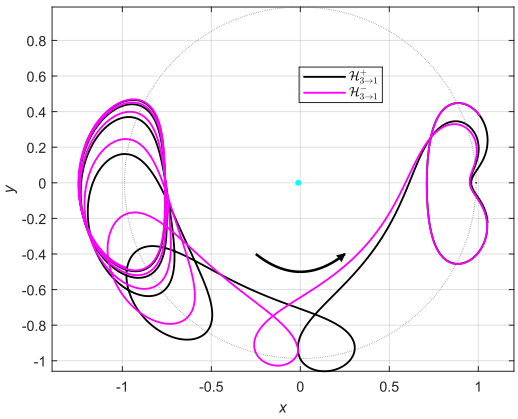

(a) The associated constructed heteroclinic trajectories, $\mathcal{H}^{\pm}_{3\to1}$, from the L_3 to the L_1 Lyapunov orbit.

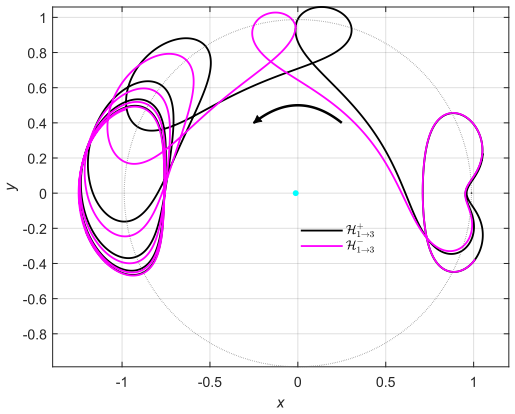

(b) The time-reversed heteroclinic trajectories, $\mathcal{H}^{\pm}_{1\to3}$, from the L_1 to the L_3 Lyapunov orbit, applying (16) to the trajectories $\mathcal{H}^{\pm}_{3\to1}$ in (a).

Figure 8: Heteroclinic Transfers $\mathcal{H}^{\pm}$ Between L_3 and L_1 Lyapunov orbits at $C = 2.9480$

TRANSFER TIME CHARACTERIZATION

Operational Zone Definition

Heteroclinic transfers between Lyapunov orbits are theoretically asymptotic connections. By construction, a stable manifold asymptotically approaches Lyapunov orbit as time $\to +\infty$, and an unstable manifold asymptotically departs the orbit as time $\to -\infty$. In other words, the spacecraft state only continuously approaches the targeted orbit and never truly reaches it in finite time.[21]Therefore, the notion of "transfer time" must be defined in a practical, operational sense.

To establish a finite transfer duration, we introduce an operational zone $\mathcal{Z}_{L_i}$ around each L_i Lyapunov orbit, representing the effective boundary of that orbit's neighborhood. This zone is defines by inflating the orbit's bounding rectangle by 5% in each coordinate direction (a $1.05\times$ scaling). The inflated bounds are then used as the axes of an ellipse centered on the orbits. The resulting elliptical region $\mathcal{Z}_{L_i}$ (around both L_1 and L_3) encloses the Lyapunov orbits, and serves as the practical areas within which the spacecraft is considered to be "on station" near that orbit. In mission terms, entering or leaving this ellipse marks the point where the spacecraft has arrived or departed from the orbit's vicinity.

Figure 9a illustrates the operational zones $\mathcal{Z}_{L_1}$ and $\mathcal{Z}_{L_3}$ as ellipses encircling their Lyapunov orbits. They are colored as gray with their their borders as dashed lines.

Transfer Time Metric and Extraction

With an operational zone established for each orbit, we quantify the time-of-flight for a heteroclinic transfer. For any trajectory $\mathcal{H}_{3\to1}$ that links the L_3 and L_1 Lyapunov orbits we define the time-of-flight,

$$t_{\text{TOF}} = t_{\text{entry}} - t_{\text{exit}} \tag{17}$$

- t_{exit} (final departure from L_3 zone). The last instant the spacecraft leaves the L_3 operational ellipse $\mathcal{Z}_{L_3}$. A trajectory on the unstable manifold may oscillate near the Lyapunov orbit and re-enter $\mathcal{Z}_{L_3}$ one or more times before committing to the transfer trajectory. Using the final exit ensures that all lingering motion inside the L_3 neighborhood is complete and the vehicle is definitively "off station."
- t_{entry} (first arrival at L_1 zone). The *first* instant the spacecraft crosses into the L_1 operational ellipse $\mathcal{Z}_{L_1}$. From that moment routine orbit-insertion activities could begin, even if the vehicle subsequently oscillates and requires additional stabilization burns.

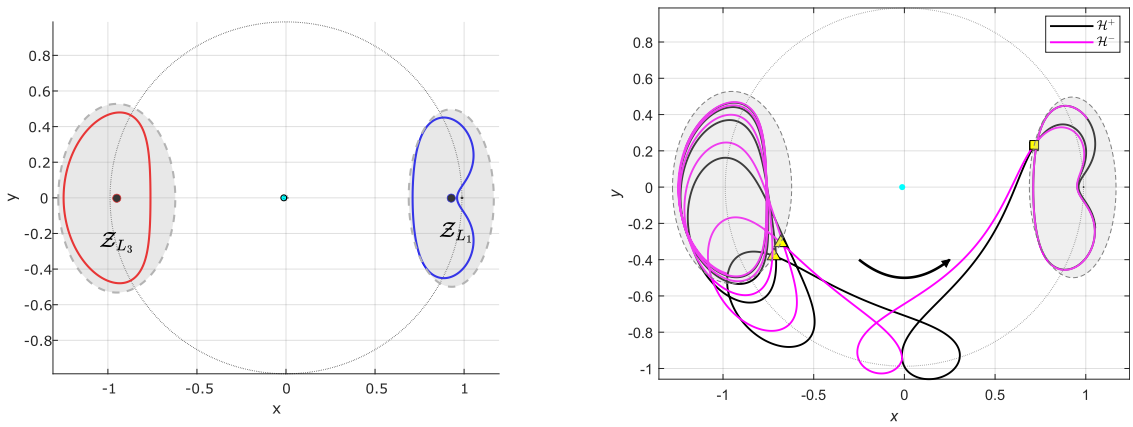

(a) Operational Zones $\mathcal{Z}_{L_1,L_3}$ in gray at $C = 2.9480$ enclosing the Lyapunov orbits.

(b) Exit and entry points marked on $\mathcal{H}^{\pm}_{3\to1}$ for the orbits in (a).

Figure 9: Operational zones and transfers.

The last-exit / first-entry rule mirrors how a flight team would handle day-to-day operations. Work in the L_3 zone continues until the vehicle leaves that region for good, so the final crossing out of $\mathcal{Z}_{L_3}$ marks the start of the transfer. Likewise, mission preparations at L_1 can begin the moment the spacecraft first slips inside $\mathcal{Z}_{L_1}$, even if it takes a few more loops to settle. By ignoring brief returns to L_3 and by not waiting for full capture at L_1, the rule isolates the time interval during which the vehicle is genuinely "in transit" between the two operational neighborhoods, giving a clear and reproducible measure of transfer duration.

It is worth noting that time-of-flight resolution in our simulation is determined by the integration accuracy rather than a fixed-step event sampling. The propagator's default settings (integration time span and step size/adaptive tolerance) were sufficient to detect the exit and entry events with acceptable accuracy in timing. In future work, one could refine the timing precision further by using event-finding algorithm or smaller step size near the boundaries of the zones but for the purposes of this analysis the current resolution is adequate.

Figure 9b shows the representative heteroclinic trajectory paths $\mathcal{H}^{\pm}_{3\to1}$, connecting L_3 and L_1 orbits. The points where the spacecraft exits $\mathcal{Z}_{L_3}$ and enters $\mathcal{Z}_{L_1}$ on each trajectory (with a yellow triangle denoting the exit point and a square denoting the entry point), illustrating how t_{TOF} is measured for each transfer.

HETEROCLINIC CONNECTIONS RESULTS AND DISCUSSION

Heteroclinic Connection Family Between L_3 and L_1 Lyapunov Orbits

We identified a continuous family of heteroclinic transfer trajectories linking L_3 Lyapunov orbits to L_1 Lyapunov orbits over a range of Jacobi Constants. In particular, using the method described in the previous sections, feasible heteroclinic transfers were found for Jacobi Constant values from approximately $C = 2.89$ to $C = 2.99$. The upper value of C was chosen to be smaller than the critical value of $C_{max} \approx 3.0015$ to ensure two distinct intersections. On the other hand, a the lower value was chosen because larger orbit amplitude would demand an enormous amount of seeding for initial conditions. In principle, the search method can be extended to even lower C values (i.e. larger Lyapunov orbits) but the computational effort grow substantially as the orbit size increase. As mentioned before, within the chosen energy window, two distinct branches of heteroclinic transfers emerge, which we label $\mathcal{H}^{+}_{3\to1}$ and $\mathcal{H}^{-}_{3\to1}$. These correspond to two different topological routes by which the unstable manifold of the L_3 orbit connects to the stable manifold of the L_1 orbit.

Figure 10 illustrates representative trajectories from each family $\mathcal{H}^{\pm}_{3\to1}$ in the rotating frame's configuration space (solid lines for the transfer segment). Figure 10a shows sample $\mathcal{H}^{+}_{3\to1}$ trajectories and Figure 10b shows

sample sample $\mathcal{H}^{-}_{3\to1}$ trajectories, each plotted in the (x, y) plane. For clarity, only 15 trajectories from each family are drawn, spanning from $C \approx 2.89$ (the largest-amplitude Lyapunov orbits considered) to $C \approx 2.99$ (the smallest Lyapunov orbits in our study). All depicted trajectories begin near L_3 Lyapunov Orbits and end near the L_1 Lyapunov orbits. The exit point from the L_3 operational zone, $\mathcal{Z}_{L_3}$, and the entry point to the L_1 operational zone,$\mathcal{Z}_{L_1}$ are marked on each trajectory (as a triangle and a square respectively in the figures), consistent with the timing definition introduced earlier.

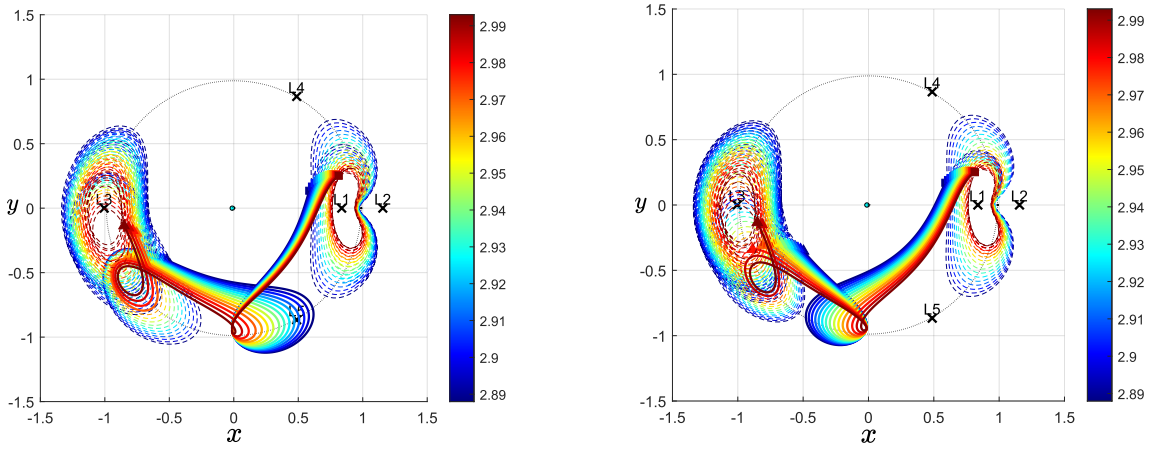

(a) $\mathcal{H}^{+}_{3\to1}$ Heteroclinic family

(b) $\mathcal{H}^{-}_{3\to1}$ Heteroclinic family

Figure 10: Heteroclinic families between L_3 and L_1

Despite the spread in energy levels, the heteroclinic transfers show an intriguing behavior when crossing $x = -\mu$. In both families, the spacecraft departs the L_3 region and swings around the vicinity of the Earth before arriving at the L_1 orbit. All trajectories cross $x \approx -\mu$ (the x-coordinate of the Earth in the rotating frame) at roughly the same location. In fact, the intersection of the stable and unstable manifolds occurs in a narrow band near $(x, y) \approx (-\mu, -0.93)$ in nondimensional units for essentially all C in this range. This indicates that the connection pathway is geometrically constrained: the stable manifold of the L_1 orbit and the unstable manifold of the L_3 orbit consistently meet in the same region of the configuration space, independent of the Lyapunov orbit size. This makes this region useful from an operation perceptive, once a spacecraft reaches that region, a small maneuver,ΔV, could be applied to transfer the spacecraft from an L_3 orbit to a different L_1 with a different C (different amplitude). It will be investigated further in future studies.

While all the heteroclinic transfers share this common "corridor" near $x = -\mu$, the two families $\mathcal{H}^{+}_{3\to1}$ and $\mathcal{H}^{-}_{3\to1}$ exhibit important qualitative differences in how they reach and use this corridor:

- $\mathcal{H}^{-}_{3\to1}$ **Family:** Trajectories in the $\mathcal{H}^{-}_{3\to1}$ branch tend to perform an extra loop on the L_3 side of the $x = -\mu$ plane before finally heading toward L_1. In practice, an $\mathcal{H}^{-}_{3\to1}$ trajectory leaving the L_3 Lyapunov orbit will first loop around before crossing the Earth's location (staying on the far side of the Poincaré section at $x = -\mu$) and only then cross the $x = -\mu$ line to travel toward the L_1 region. This behavior can be seen in Figure 10b, where the paths initially curve around on the left side of the figure before moving rightwards. The size of this loop on the L_3 side is correlated with the Jacobi constant: lower C (i.e. larger Lyapunov orbits) produces a more pronounced and wider loop, whereas at higher C (smaller orbits) the loop is tighter. In summary, the $\mathcal{H}^{-}_{3\to1}$ heteroclinic transfers spend more time in the far side of the Moon's region, looping around at least once in the L_3 vicinity, before proceeding to L_1.
- $\mathcal{H}^{+}_{3\to1}$ **Family:** Trajectories in the $\mathcal{H}^{+}_{3\to1}$ branch follow a different route. They tend to cross the $x = -\mu$ plane more directly from the L_3 side and then execute their looping on the L_1 side of that plane. As shown in Figure 10a, an $\mathcal{H}^{+}_{3\to1}$ trajectory departs L_3 and almost immediately transitions through the

$x = -\mu$ section to the Earth-Moon side, where it then loops around in the vicinity of the Moon's side of the system before approaching L_1. The loops associated with $\mathcal{H}^+_{3\to1}$ transfers are generally larger in extent than those of the $\mathcal{H}^-_{3\to1}$ family for the same energy level, meaning that an $\mathcal{H}^+_{3\to1}$ trajectory at a given C will swing out further during its loop than the corresponding $\mathcal{H}^-_{3\to1}$ trajectory. Furthermore, at the lower end of our Jacobi constant range (closer to $C = 2.89$), some $\mathcal{H}^+_{3\to1}$ trajectories loop so far out on the L_1 side that they come near the vicinity of the L_5 Lagrange point before turning back toward the L_1 orbit. In these cases, the trajectory temporarily ventures into the region around L_5 as part of its path. This is a distinguishing feature of the $\mathcal{H}^+_{3\to1}$ family – for smaller C values, the transfer orbit can effectively "visit" the neighborhood of L_5 on its way to L_1, whereas $\mathcal{H}^-_{3\to1}$ orbits do not.

These geometric differences between the $\mathcal{H}^-_{3\to1}$ and $\mathcal{H}^+_{3\to1}$ families could be useful from a mission design perspective. The existence of two distinct routes offers flexibility in planning transfers depending on mission objectives. For example, if a mission planner prefers a trajectory that stays longer on the far side of the Moon (or the far side of Earth, in the rotating frame) – perhaps for extended observations – then an $\mathcal{H}^-_{3\to1}$ transfer would be the natural choice, since it loops behind the Earth in the rotating frame before heading to L_1. On the other hand, if the goal is to incorporate a swing past the L_5 region or generally to spend more time on the Moon's side of the system during the transfer, an $\mathcal{H}^+_{3\to1}$ trajectory would be more appropriate, as it carries the spacecraft through the L_1 side loop (potentially near L_5) en route to the L_1 orbit. In summary, the two heteroclinic families $\mathcal{H}^-_{3\to1}$ and $\mathcal{H}^+_{3\to1}$ represent two different natural "highways" in the Earth–Moon phase space, each with its own characteristic path.[4,22] Recognizing and understanding these path differences enables mission designers to select the transfer that best aligns with the desired route and scientific objectives of the mission.

Transfer Time Analysis

In the Earth–Moon circular restricted three-body problem (CR3BP), we use nondimensional units where the primary orbital period is 2π. One time unit in this normalized system corresponds to approximately 4.345 days. For clarity, all transfer times (t_{TOF}) are converted to days using this factor ($t_{\mathrm{days}} = 4.345\ t_{\mathrm{nd}}$). This means that a dimensionless time of 2π (one Earth–Moon revolution) is about 27.3 days in physical units. Since the transfer time for the computed heteroclinic transfers and their time reversed version is the same, we will refer to the combined family as $\mathcal{H}^{\pm}$, where $\mathcal{H}^{\pm} = \mathcal{H}^{\pm}_{3\to1} \bigcup \mathcal{H}^{\pm}_{1\to3}$.

Figure 11 shows the total transfer time (time-of-flight from departure of L_3 zone to arrival at L_1 zone) as a function of the Jacobi constant C for the two heteroclinic families ($\mathcal{H}^-$ in blue and $\mathcal{H}^+$ in red). Several notable features can be observed from this plot:

- **Discontinuities at high C values:** Both time-of-flight curves exhibit a sharp jump (discontinuity) at a certain Jacobi constant. In particular, the $\mathcal{H}^-$ curve jumps around $C \approx 2.98$, and the $\mathcal{H}^+$ curve around $C \approx 2.97$. This abrupt increase is an artifact of our operational zone exit/entry definitions. At these higher C (smaller Lyapunov orbits), the trajectory leaving L_3 performs an extra loop entirely outside the L_3 operational zone before finally entering the transfer route. According to our timing rule, this entire loop gets counted in the transfer duration. For slightly lower C (larger orbits), a similar looping occurs but it enters the L_3 zone partway, meaning the spacecraft is considered to still be in operation before completing the loop – thereby excluding that loop from the transfer time. It can be seen in Figure 10 where trajectories with higher C values tend to start the transfer earlier than the lower C values. The net effect is that beyond these threshold Jacobi values, the transfer time suddenly increases by roughly the period of an L_3 Lyapunov orbit ($\approx 27 - 28$ days). Indeed, we find the size of the jump in each curve is approximately equal to one L_3 orbit period, confirming that the discontinuity corresponds to the inclusion of one additional loop in the transfer trajectory.

- **Transfer time increases with C:** Aside from the discrete jumps, the overall trend is that transfer time grows steadily with increasing Jacobi constant for both families. In the energy window $C \approx 2.89$ to 2.99, higher C (i.e. smaller-amplitude Lyapunov orbits) consistently yields longer flight times. For example, at the low end of this range ($C \approx 2.89$ corresponding to the largest orbits considered), the

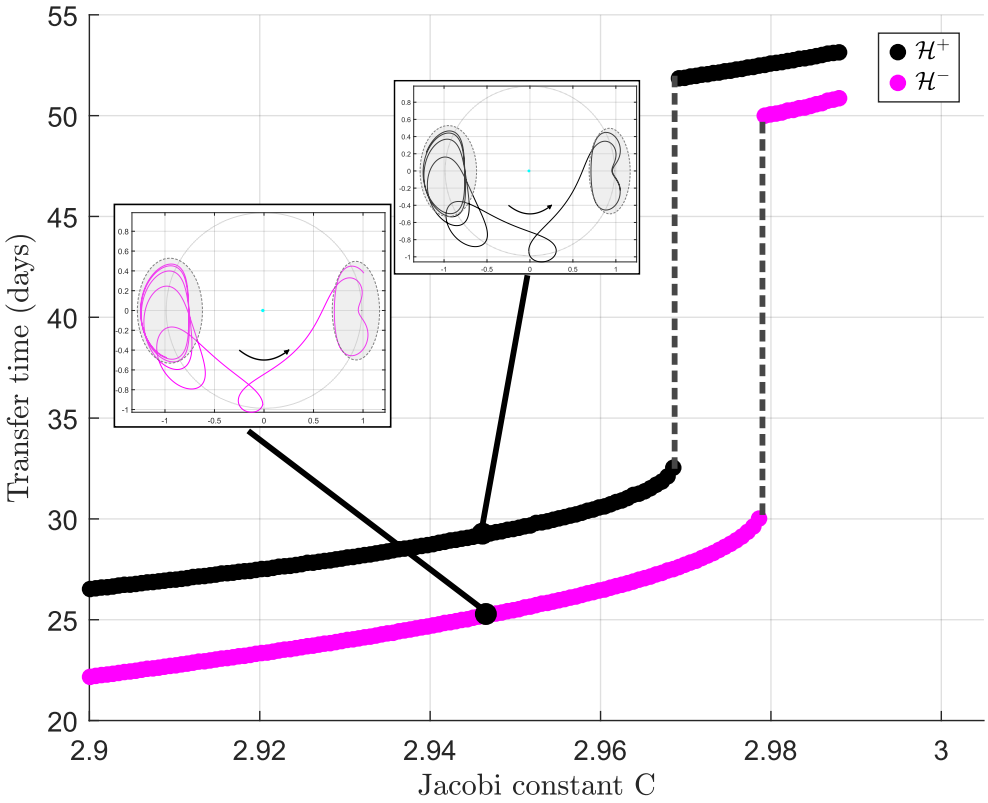

Figure 11: Transfer time t_{TOF} in days vs. Jacobi constant C

heteroclinic transfers are the quickest. At the high end ($C \approx 2.99$, smallest orbits), the time-of-flight is longer. This monotonic increase makes intuitive sense: higher C value have smaller Lyapunov orbits amplitude which would lead to smaller operational zones $\mathcal{Z}$. Therefore, the distance the spacecraft has to travel further between the operational zones, so they naturally take more time to complete the transfer. Thus, within our study's range, raising the Jacobi constant leads to a longer transfer duration (with the only exception being the sudden jump discussed above).

- **$\mathcal{H}^-$ and $\mathcal{H}^+$ time offset:** For any given Jacobi constant in this family, $\mathcal{H}^-$ transfers are consistently faster (shorter time-of-flight) than $\mathcal{H}^+$ transfers. The two curves in Figure 11 remain roughly parallel across the range, with the $\mathcal{H}^+$ curve about 4–5 days above the $\mathcal{H}^-$ curve at almost every C. In other words, an $\mathcal{H}^+$ transfer typically takes 4.5 days longer than the corresponding $\mathcal{H}^-$ transfer. This nearly constant time gap can be traced to the route geometry described earlier. As discussed in the previous subsection, $\mathcal{H}^+$ trajectories cross the $x = -\mu$ Poincaré section more directly and then execute a larger loop on the L_1 side (often swinging out toward the vicinity of L_5 for lower C values). In contrast, $\mathcal{H}^-$ trajectories spend more time looping on the L_3 side and take a somewhat more direct path once they cross to the L_1 side. The longer, more expansive loop in the $\mathcal{H}^+$ family adds extra distance and duration to those transfers, explaining why $\mathcal{H}^+$ missions consistently require a few additional days of travel compared to $\mathcal{H}^-$ missions.

In summary, the transfer time analysis reinforces the distinction between the two heteroclinic families. Not only do $\mathcal{H}^-$ and $\mathcal{H}^+$ follow different spatial routes, but they also entail different time-of-flight profiles: $\mathcal{H}^-$ provides a faster transfer, whereas $\mathcal{H}^+$ offers an alternative path at the cost of a longer travel time. This gives mission designers a clear trade-off – one can choose the shorter transfer of $\mathcal{H}^-$ or opt for the $\mathcal{H}^+$ route (with its unique looping near the L_5 region) if the mission objectives favor that trajectory, accepting the roughly 4–5 day additional time-of-flight. Such flexibility in the natural dynamics can be crucial in mission planning, allowing the route to be tailored to both time constraints and desired scientific/operational goals.

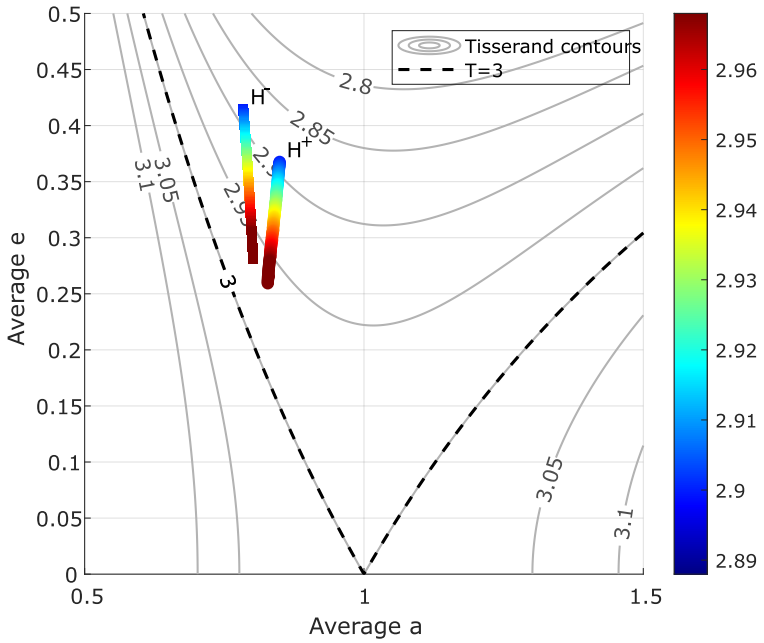

Figure 12: Averaged orbital elements on Tisserand Contours

Orbital Elements Analysis

To further characterize the heteroclinic transfers identified in this study, we examine the orbital elements of each trajectory along its transfer arc, focusing on the average semimajor axis (a) and eccentricity (e) relative to Earth. The spacecraft states, originally computed in the rotating frame, are first transformed into the Earth-centered inertial (ECI) frame, then converted into approximate conic elements under the two-body (Keplerian) assumption. These elements are sampled along each trajectory and averaged over the full transfer duration, excluding segments inside the operational zones, $\mathcal{Z}_{L_3}, \mathcal{Z}_{L_1}$.

Figure 12 shows the resulting distribution of (a, e) values for the $\mathcal{H}^+$ and $\mathcal{H}^-$ families, overlaid on contours of the Earth-relative Tisserand Parameters, an approximation to the Jacobi constant in orbital element space. Notably, the $\mathcal{H}^-$ family exhibits consistently lower average semimajor axes than the $\mathcal{H}^+$ family, a result that aligns with the transfer time analysis discussed earlier: lower a corresponds to trajectories that remain closer to Earth on average, which in turn moves the spacecraft faster, resulting in a faster transfer. This observation reinforces the dynamical distinction between the two families $\mathcal{H}^+$ and $\mathcal{H}^-$.

A second observation concerns the Tisserand contours. As shown in Figure 12, the averaged orbital elements are above the $T = 3$ contour. Therefore, they are in a regime where transit between gravitational region is possible. This is consistent with opening and closing of the L_1 and L_3 gateways which makes the heteroclinic transfers feasible.

Figure 13 further illustrates a representative heteroclinic trajectory in both the rotating and inertial frames. The left panel shows the path in the rotating frame, where the dashed curve trajectory in the operational zones, the solid line is the transfer segment, and the green and red dots are the exit and entry points respectively. The right panel reveals the same trajectory in the inertial frame, clearly demonstrating that the motion is non-Keplerian throughout: the path does not trace a simple ellipse, and instead exhibits continuous rotation and precession. This behavior confirms that the three-body gravitational effects are dynamically active over the entire transfer, and the conic elements (e.g. $a(t), e(t)$) are varying along the arc.

CONCLUSION

Driven by the growing interest in deep-space exploration and the development of cislunar infrastructure, as well as the underexplored potential of the Earth–Moon L_3 region,[12,16,17] this study investigated low-energy

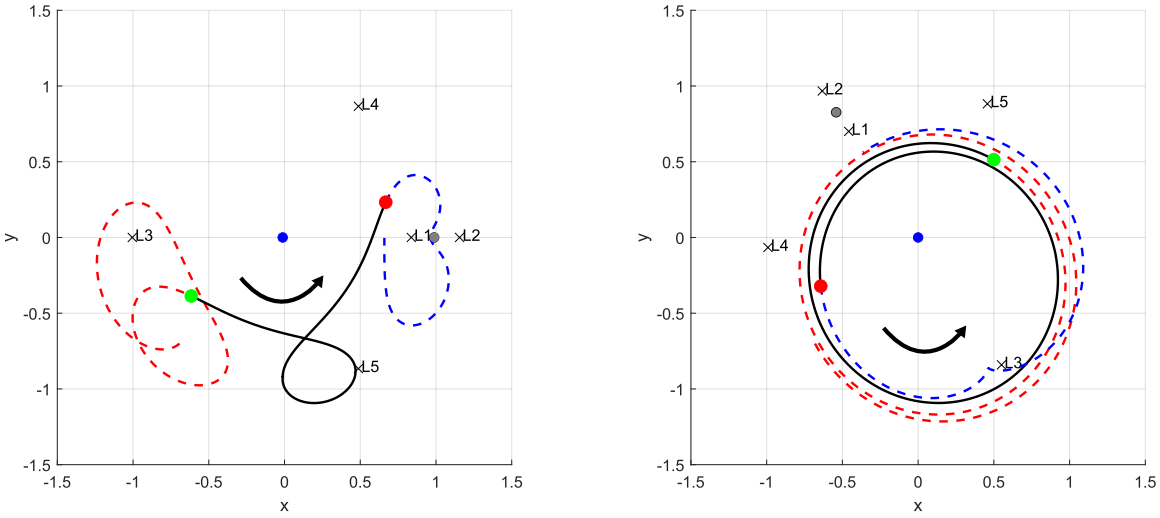

(a) $\mathcal{H}^{+}_{3\to1}$ Heteroclinic Trajectory at $C = 2.93$ in the rotating frame

(b) $\mathcal{H}^{+}_{3\to1}$ Heteroclinic Trajectory at $C = 2.93$ in the inertial frame

Figure 13: Rotating and Inertial frame representative trajectory

transfers between L_1 and L_3 Lyapunov orbits. We have demonstrated, for the first time, the existence of heteroclinic connections linking periodic Lyapunov orbits around Earth–Moon L_1 and L_3. By leveraging the planar CR3BP model, we identified two continuous families of such transfers (denoted $\mathcal{H}^{-}$ and $\mathcal{H}^{+}$), thereby addressing a key gap in multi-body trajectory design and expanding the toolbox of ballistic cislunar routes.[23–25]

The two heteroclinic families exhibit distinct geometries and time-of-flight characteristics. Using an enhanced multi-crossing Poincaré map technique, we captured all relevant manifold intersections on the section, revealing the complete intersection geometry and enabling the systematic construction of both $\mathcal{H}^{-}_{3\to1}$ and $\mathcal{H}^{+}_{3\to1}$ trajectories. The $\mathcal{H}^{+}_{3\to1}$ transfers tend to include a wide looping arc on the near-moon side, L_1 region (often reaching toward the L_5 vicinity), whereas $\mathcal{H}^{-}_{3\to1}$ transfers spend more time on the far side (L_3 region) before transitioning. These geometric differences translate into different timing profiles: for a given energy (Jacobi constant), $\mathcal{H}^{-}_{3\to1}$ transfers are consistently faster, typically achieving shorter flight times by about 4–5 days compared to their $\mathcal{H}^{+}_{3\to1}$ counterparts.

Our analysis of transfer duration as a function of Jacobi constant revealed a clear trend: higher Jacobi constants (smaller-amplitude orbits) yield longer flight times, while lower values (larger orbits) produce quicker transfers. This monotonic increase in time-of-flight is marked by discrete jumps in duration; each jump adding roughly one L_3 orbit period ($\approx$ 28 days). These jumps occur because of our operational zone, $\mathcal{Z}$, definitions: when a trajectory executes an extra loop entirely outside the L_3 zone, $\mathcal{Z}_{L_3}$, before final exit, that loop is counted in the transfer time; for slightly larger orbits that loop is partly inside the zone, and the loop is excluded from the transfer time. Aside from these zone-definition–induced discontinuities, the $\mathcal{H}^{-}_{3\to1}$ family consistently achieves a shorter time-of-flight than $\mathcal{H}^{+}_{3\to1}$ across the entire energy range. These results highlight a meaningful trade-off between the two routes and underscore how energy level and zone definitions influence transfer efficiency.

Practically, the existence of low-energy L_1–L_3 heteroclinic transfers carries significant implications for mission design. It provides a new pathway to reposition spacecraft between near the moon and far from the moon periodic orbits without the need for large propulsive maneuvers or insertion burns at the destination. For example, an asset stationed in an L_1 halo orbit (such as a Gateway platform or communications relay) could be transferred into an L_3 orbit ballistically, allowing it to take up a strategic vantage point behind the Earth with minimal fuel expenditure. This capability enhances operational agility in cislunar space: it enables cislunar surveillance or communication platforms at L_3 to be deployed and serviced from L_1, and it offers a

way to redistribute spacecraft among libration-point orbits in response to evolving mission needs, all while leveraging natural dynamics.

Furthermore, our results help open the Earth–Moon L_3 region as a useful staging area for advanced missions. Because of L_3's quasi-stable nature, it can maintain objects in the vicinity with very small correction maneuvers. This suggests that L_3 could serve as a capture point for interplanetary material or a logistics hub in the future. For instance, a captured near-Earth asteroid might be inserted into a stable L_3 orbit by aligning with L_3's stable manifold, as earlier analyses have hinted, requiring only a very small ΔV. Similarly, lunar or deep-space supply depots could be positioned at L_3 and reached via ballistic transfers from L_1 or L_2. The two families of trajectories identified in this work give mission planners flexibility to choose between a faster transfer ($\mathcal{H}^{-}_{3\to1}$) or a longer transfer ($\mathcal{H}^{+}_{3\to1}$) that might cover different spatial regions; a choice that can be made based on mission priorities such as time constraints or scientific observation needs.

Looking ahead, several directions for future research are identified:

1. **Sensitivity and Robustness Analysis:** Ongoing and future work will examine how sensitive the L_1–L_3 heteroclinic trajectories are to small perturbations and realistic mission constraints. This effort will quantify the tolerance to initial manifold-targeting errors, finite-thrust maneuver deviations, timing mismatches, and launch-window shifts, and will determine the necessary station-keeping or guidance corrections. By combining sensitivity studies with robustness testing—under both idealized perturbations and practical navigation errors—we will assess how much ΔV or control authority is required to maintain the heteroclinic transfer in real-world operations.

2. **Improved intersection precision:** We plan to refine the heteroclinic trajectory computation by increasing the precision of manifold intersection targeting. Techniques such as high-order curve fitting of manifold trajectories or differential correction algorithms can be applied to achieve more exact intersections between stable and unstable manifolds. Improving this intersection precision will reduce any insertion errors, minimize the ΔV needed for cleanup maneuvers, and possibly uncover additional transfer solutions that were missed with the current resolution.

3. **Extension to 3D models:** The next step is to explore heteroclinic connections in higher-fidelity dynamical models. This involves extending the analysis to the spatial (3D) CR3BP and the bicircular four-body problem to assess whether similar L_1–L_3 transfer families exist when out-of-plane motion and solar gravitational perturbations are included. Verifying the persistence of these transfers in a 3D setting will be crucial for actual mission design.

4. **Utilizing L_3 as a staging point for asteroid capture and logistics:** Finally, we will investigate mission concepts that leverage Earth–Moon L_3 as a staging hub. This entails analyzing scenarios where a small asteroid or other payload is delivered to L_3 orbit (for example, via a heteroclinic transfer from a translunar trajectory) and held there for exploration or resource utilization. Additionally, we will consider how L_3 could function in a network of cislunar logistics—for instance, as an intermediate storage orbit for fuel or supplies, or as a relay location—and what role the identified low-energy transfers would play in establishing and sustaining such an infrastructure

In summary, this work confirms that ballistic heteroclinic transfers between L_1 and L_3 are feasible and provides a first characterization of their families and properties. These results not only fill a notable gap in cislunar trajectory research but also lay a foundation for expanding future mission architectures to include the Earth–Moon L_3 point. With continued research addressing the above directions, we expect the L_3 hub to become an attractive option in the design of future deep-space missions and cislunar operations.

ACKNOWLEDGMENT

We thank Mark Munson for pointing out the potential utility of the Earth-Moon L_3 region. This research was partially supported by funding from the AFOSR under Award No. FA9550-24-1-0194. Travel support to this conference was provided by the Saudi Arabian Cultural Mission.

REFERENCES

[1] NASA, "Gateway Overview," https://www.nasa.gov/gateway, 2025.

[2] D. D. Mazanek, R. G. Merrill, J. R. Brophy, and R. P. Mueller, "Asteroid Redirect Mission concept: A bold approach for utilizing space resources," *Acta Astronautica*, Vol. 117, 2015, pp. 163–171, https://doi.org/10.1016/j.actaastro.2015.06.018.

[3] M. Patel, Y. Shimane, H. W. Lee, and K. Ho, "Cislunar Satellite Constellation Design via Integer Linear Programming," *The Journal of the Astronautical Sciences*, Vol. 71, No. 3, 2024, p. 26, 10.1007/s40295-024-00445-8.

[4] S. D. Ross, "The interplanetary transport network," *American Scientist*, Vol. 94, 2006, pp. 230–237.

[5] D. C. Davis, E. Zimovan-Spreen, R. Power, and K. C. Howell, "Cubesat Deployment from a Near-Rectilinear Halo Orbit," *AIAA SciTech Forum*, San Diego, California, AIAA, January 3–7 2022.

[6] W. Koon, M. Lo, J. Marsden, and S. Ross, "Heteroclinic Connections Between Periodic Orbits and Resonance Transitions in Celestial Mechanics," *Chaos (Woodbury, N.Y.)*, Vol. 10, 07 2000, pp. 427–469, 10.1063/1.166509.

[7] P. Pergola and E. M. Alessi, "Libration point orbit characterization in the Earth–Moon system," *Monthly Notices of the Royal Astronomical Society*, Vol. 426, 10 2012, pp. 1212–1222, 10.1111/j.1365-2966.2012.21585.x.

[8] T. Pavlak and K. Howell, "Strategy for Optimal, Long-Term Stationkeeping of Libration Point Orbits in the Earth-Moon System," *AIAA/AAS Astrodynamics Specialist Conference 2012*, 08 2012, 10.2514/6.2012-4665.

[9] D. Henry and D. Scheeres, "A Survey of Heteroclinic Connections in the Earth-Moon System," *International Astronautical Congress*, 09 2022.

[10] D. Folta, M. Woodard, and D. Cosgrove, "Stationkeeping of the First Earth-Moon Libration Orbiters - The ARTEMIS Mission," *Advances in the Astronautical Sciences*, Vol. 142, 01 2011.

[11] D. Folta and F. Vaughn, "A Comprehensive Survey of Earth-Moon Libration Orbits: Stationkeeping Strategies And Intra-Orbit Transfers," *Collection of Technical Papers - AIAA/AAS Astrodynamics Specialist Conference*, Vol. 1, 02 2004, 10.2514/6.2004-4741.

[12] J. Dahlke, A. Wilmer, and R. Bettinger, "Preliminary Comparative Assessment of L2 and L3 Surveillance Using Select Cislunar Periodic Orbits," *AAS/AIAA Astrodynamics Specialist Conference, 1-19*, 08 2022.

[13] M. Conti and C. Circi, "Design of halo orbit constellation for lunar global positioning and communication services," *Astrodynamics*, Vol. 9, May 2025, pp. 231–245, 10.1007/s42064-024-0220-x.

[14] Y. Liang, B. Nicolás, and Jorba, "Leveraging L3 to transfer to L4 in the Sun-perturbed Earth-Moon system," *Acta Astronautica*, Vol. 189, 2021, pp. 337–348, https://doi.org/10.1016/j.actaastro.2021.08.034.

[15] E. A. Evans, M. J. Holzinger, and D. J. Scheeres, "An Investigation of Impulsive-Maneuver Transfers from L3, L4 and L5 to Earth-Orbit," *Proceedings of the 25th Advanced Maui Optical and Space Surveillance Technologies Conference*, Wailea Beach Resort, Maui, Hawaii, September 2024.

[16] M. A. Munson Jr, *Using the Circular Restricted Three-Body Problem to Design an Earth-Moon Orbit Architecture for Asteroid Mining*. PhD thesis, Virginia Tech, 2024.

[17] Jorba and B. Nicolás, "Using Invariant Manifolds to Capture an Asteroid near the L3 Point of the Earth–Moon Bicircular Model," *Communications in Nonlinear Science and Numerical Simulation*, Vol. 102, 2021, p. 105948, 10.1016/j.cnsns.2021.105948.

[18] Jet Propulsion Laboratory, California Institute of Technology, "Three-Body Periodic Orbits Tool," https://ssd.jpl.nasa.gov/tools/periodic_orbits.html#/intro, 2025. Accessed: 2025-07-10.

[19] W. S. Koon, M. W. Lo, J. E. Marsden, and S. D. Ross, *Dynamical Systems, the Three-Body Problem and Space Mission Design*. Marsden Books, 2 ed., 2022.

[20] G. Gomez, A. Jorba, J. Masdemont, and C. Simó, *Dynamics and mission design near libration points, advanced methods for collinear points*. World Scientific Publishing Company, 02 2001, 10.1142/4337.

[21] S. H. Strogatz, *Nonlinear Dynamics and Chaos: With Applications to Physics, Biology, Chemistry, and Engineering*. Reading, MA: Perseus Books, 1994.

[22] F. Reddy, "How scientists discovered a solar system "superhighway"," *Astronomy*, Vol. 36, 2008, pp. 38–43.

[23] E. A. Belbruno, "The dynamical mechanism of ballistic lunar capture transfers in the four-body problem from the perspective of invariant manifolds and Hill's regions," *Centre de Recera Matemàtica, Institut D'Estudis Catalans*, Preprint No. 270, 1994.

[24] W. S. Koon, M. W. Lo, J. E. Marsden, and S. D. Ross, "Low energy transfer to the Moon," *Celestial Mechanics and Dynamical Astronomy*, Vol. 81, 2001, pp. 63–73.

[25] M. W. Lo and S. D. Ross, "The Lunar L1 Gateway: Portal to the stars and beyond," *AIAA Space 2001 Conference*, Albequerque, New Mexico, 2001.